Journal of Nanobiotechnology

RESEARCH

Open Access

Polypyrrole-ferric phosphate-methotrexate nanoparticles enhance apoptosis/ferroptosis of M1 macrophages via autophagy blockage for rheumatoid arthritis treatment

Hui Liu[1,2,3,6], Haoyu Wan[1,2], Anbiao Zhang[1,2], Yi Ouyang[3], Xinya Lu[1,2], Mengyuan Wu[3], Ning Hu[4], Jianying Pan[1,2*], Dong Guo[1,2*], Zhong Alan Li[5*] and Denghui Xie[1,2*]

Abstract

Rheumatoid arthritis (RA) is an inflammatory disease that progresses from synovial inflammation to cartilage and bone destruction. Eliminating pro-inflammatory M1 macrophages is a promising strategy for RA treatment, but is impeded by cytoprotective autophagy. Herein, we report an effective autophagy blockage-promoted apoptosis/ferroptosis strategy using multifunctional ferric phosphate-decorated, methotrexate-loaded polypyrrole nanoparticles (PPy-FePi-MTX NPs) to achieve enhanced RA treatment effects. When injected into the knee joints of a collagen-induced DBA/1J mouse model of RA, the payloads on PPy NPs are released under the stimulation of an inflammatory microenvironment. The released MTX can directly induce M1 macrophage apoptosis. Upon near-infrared laser irradiation, the photothermal effect of PPy NPs further promotes cellular apoptosis. In addition, Fe^{3+} reacts with intracellular over-expressed glutathione to form Fe^{2+}, which can convert hydrogen peroxide into toxic hydroxyl radicals. This redox process could deplete glutathione, inactivate glutathione peroxidase 4, and cause lipid peroxidation accumulation, resulting in ferroptosis of inflammatory M1 macrophages. Furthermore, PO_4^{3-} disrupts the normal function of lysosomes by pH disturbance, disabling the cytoprotective autophagy of M1 macrophages for enhanced anti-RA effects. This work develops multifunctional PPy NPs for RA treatment through effective elimination of pro-inflammatory M1 macrophage.

Keywords Autophagy blockage, Apoptosis, Ferroptosis, Rheumatoid arthritis, Photothermal therapy

*Correspondence:
Jianying Pan
storm0132002@163.com
Dong Guo
19927472465@163.com
Zhong Alan Li
Alanli@cuhk.edu.hk
Denghui Xie
smuspine@163.com
[1]Department of Orthopedic Surgery, Center for Orthopedic Surgery, The Third Affiliated Hospital, Southern Medical University, Guangzhou 510630, PR China
[2]Guangdong Provincial Key Laboratory of Bone and Joint Degeneration Diseases, Guangzhou 510630, PR China
[3]Key Laboratory of Luminescence Analysis and Molecular Sensing (Southwest University), Ministry of Education, School of Materials and Energy, Southwest University, Chongqing 400715, PR China
[4]Department of Orthopaedics, The First Affiliated Hospital of Chongqing Medical University, Chongqing 400016, PR China
[5]Department of Biomedical Engineering, The Chinese University of Hong Kong, Hong Kong, NT, PR China
[6]State Key Laboratory of Molecular Engineering of Polymers, Fudan University, Shanghai 201199, PR China

Introduction

Rheumatoid arthritis (RA) is a chronic inflammatory autoimmune disorder that impacts approximately 1% of the global population, which are characterized by synovial hyperplasia and inflammation, pannus formation, cartilage damage, and bone erosion [1, 2]. The progressive inflammation and persistent synovitis in RA lead to structural and functional destruction of bone and cartilage [3]. Various inflammatory cells, particularly M1 macrophages, secrete pro-inflammatory cytokines and cause pannus formation in RA joints, mediating tissue damage and erosion in the late stage [4–6]. Therefore, eliminating M1 macrophages using effective therapeutic strategies represents a promising approach to realizing desirable RA treatment.

Apoptosis and ferroptosis pathways have been well studied for disease treatment [7–10]. Apoptosis is a kind of caspase-dependent programmed cell death that can be initiated by chemical drugs, photothermal agents under near-infrared (NIR) light irradiation, and reactive oxygen species (ROS) [11–16]. Ferroptosis features iron overload-mediated lipid peroxidation (LPO) accumulation [17]. During this process, ferrous ions convert hydrogen peroxide (H_2O_2) into toxic hydroxyl radicals (·OH) to destroy intracellular redox balance to cause cell death [18, 19]. As ferroptosis is featured by high intracellular oxidative stress, the outcome of ferroptosis is influenced by the levels of H_2O_2 and reducing substances in cells [20]. The combination of apoptosis and ferroptosis has been proven to show superiority in disease therapies to apoptosis or ferroptosis alone [21, 22]. However, the therapeutic efficacy of combined apoptosis and ferroptosis strategies has always been compromised by cytoprotective resistance.

Autophagy is a typical cytoprotective process, in which cells eliminate the damaged biomacromolecules and organelles through the lysosome-mediated digestion process [23, 24]. This process could maintain cell survival under internal and external stimuli-caused detrimental conditions [25]. The cellular damages generated in treatments can activate the autophagy mechanism to compromise therapeutic efficacy and enhance the cellular resistance to death [26–28]. Thus, to effectively manage RA pathogenesis and progression, it is crucial to regulate the survival rate of immune cells. Autophagy process is considered a protective mechanism of synovial cells, inhibiting which could promote synovial cell death with high efficiency [29, 30]. Therefore, strategies for cytoprotective autophagy blockage are expected to enhance anti-RA therapeutic efficacy.

The design and development of multifunctional nanomaterials that integrate therapeutic functions and autophagy blockage capacity using facile methods are promising strategies for effective RA treatment. Herein, we report an effective autophagy blockage-promoted apoptosis/ferroptosis strategy, realized by using multifunctional ferric phosphate-decorated and methotrexate-loaded polypyrrole nanoparticles (PPy-FePi-MTX NPs), for enhanced RA treatment. When located in inflammation regions, the payloads on PPy NPs are released under the stimulation of an inflammatory microenvironment. PPy NPs can serve as photothermal agents, generating hyperthermia upon NIR laser irradiation to promote M1 macrophage apoptosis [31, 32]. As a kind of first-line antirheumatic drug, the released MTX can inhibit the recruitment and proliferation of M1 macrophages, inducing direct damage [33, 34]. Fe^{3+} reacts with intracellular over-expressed glutathione (GSH, a kind of important intracellular antioxidant [35, 36]) to form Fe^{2+}, which could convert H_2O_2 into toxic ·OH, causing apoptosis and ferroptosis simultaneously [37, 38]. This redox process could deplete GSH, inactivate glutathione peroxidase 4 (GPX4), and cause lipid peroxidation (LPO) accumulation, resulting in ferroptosis of inflammatory M1 macrophages. Notably, PO_4^{3-} disrupts the normal function of lysosomes by pH disturbance, disabling the cytoprotective autophagy of M1 macrophages for enhanced anti-RA efficacy [39]. This work not only develops an effective strategy for anti-RA treatment, but also underscores the key role of autophagy blockage in enhancing the therapeutic outcome.

Materials and methods

Preparation of PPy-FePi-MTX NPs

First, polyvinyl alcohol (PVA, 12 mg/mL, 15 mL) aqueous solution was mixed with $FeCl_3$ (0.83 g) under agitation in an ice bath. After 1 h, pyrrole (100 μL) was added to the mixture. This reaction was carried out for 5 h, and then this mixture was purified by centrifugation to obtain PPy-Fe NPs. For drug loading, MTX (1 mg/mL, 18 mL) in PBS was mixed with an aqueous solution of PPy-Fe NPs (2 mg/mL, 36 mL) on a shaker (100 rpm, at room temperature) for 12 h and centrifuged to obtain PPy-FePi-MTX NPs. For comparison, MTX in ammonia solution was also mixed with PPy-Fe NPs using a similar method to form PPy-Fe-MTX NPs.

Photothermal performance evaluation

The photothermal stability of PPy-FePi-MTX NPs (400 ppm) was tested by 4 repeated laser-on/off cycles (1064 nm, 1.0 W/cm^2, 5 min on, 15 min off). A series of aqueous solutions of PPy-FePi-MTX NPs in a concentration gradient (0, 25, 50, 100, 200, and 400 ppm) were irradiated with the same laser (5 min, 1.0 W/cm^2) to record the temperature values. Moreover, aqueous solutions of PPy-FePi-MTX NPs at 400 ppm were irradiated with the same laser (10 min, 1.0 W/cm^2) and cooled down for 20 min to collect the temperature curve. Then, the

photothermal conversion efficiency of PPy-FePi-MTX NPs was calculated.

Collagen-induced arthritis (CIA) model and biocompatibility assessment

Male DBA/1J mice (7–8 weeks old, 20 ± 2 g) were obtained from GemPharmatech (Nanjing, China) and maintained in a sterile environment with free access to food and water. The animal experiments were approved by the Animal Experimental Committee of Daoke Pharmaceutical Technology (Guangdong) Co., Ltd (Approval IACUC-DK-2024-01-01-01) and complied with the National Law on Experimental Animal Utilization (People's Republic of China).

The CIA mouse model was established by emulsifying 2 mg/mL bovine type II collagen with Complete Freund's Adjuvant to form mixture A and with Incomplete Freund's Adjuvant to form mixture B. These mixtures were stirred overnight in a cold water bath. On day 0, DBA/1J mice were subcutaneously injected with 0.1 mL of mixture A via the tail, followed by a booster injection of mixture B on day 21. Arthritis progression was assessed every three days. Following the establishment of the CIA model, the mice were divided into seven groups: sham, PBS plus laser, MTX, PPy-Fe plus laser, PPy-Fe-MTX plus laser, PPy-FePi-MTX plus laser, and PPy-FePi-MTX ($n = 8$ per group). The mice in the treatment groups received weekly intra-articular injections (10 μL, 200 ppm) for 6 weeks and subsequently exposed to 1.0 W/cm^2 1064 nm laser for 5 min. Sixty days after the initial immunization, the mice were euthanized, and their knee joints were collected for micro-CT scanning and histological analysis.

To evaluate the biocompatibility of various NPs, serum samples were collected from mice post-treatment. The concentrations of aspartate aminotransferase (AST), alanine aminotransferase (ALT), blood urea nitrogen (BUN), and creatinine (Cre) were measured utilizing standard assay kits, following the protocols specified by the manufacturer.

Detection of intracellular reactive oxygen species (ROS) and apoptosis

For ROS detection, RAW 264.7 cells were cultured in 24-well plates overnight. Subsequently, the cells were subjected to treatments with PPy-Fe NPs, PPy-Fe-MTX NPs, or PPy-FePi-MTX NPs for 6 h, followed by exposure to laser irradiation at a wavelength of 1064 nm and a power density of 1.0 W/cm^2 for a duration of 5 min. The control group underwent treatment with phosphate-buffered saline (PBS). Following this, 10 μM of ROS probe DCFH-DA was introduced into each group. Following a 30-min incubation period, the cells were rinsed thrice with PBS. The images were captured by using an inverted Olympus microscope.

For apoptosis detection, RAW 264.7 cells were cultured in 6-well plates overnight. Following the aforementioned cellular treatments, apoptosis analysis was conducted through flow cytometry, utilizing Annexin V-fluorescein isothiocyanate (AV-FITC) and propidium iodide (PI) double-staining.

Detection of intracellular glutathione (GSH)

For glutathione detection, LPS-treated RAW 264.7 cells were collected, washed twice with PBS, resuspended in 0.3–0.5 mL isotonic PBS (0.1 M, pH 7.4), and disrupted by sonication. Subsequently, 0.1 mL homogenate was combined with 0.1 mL reagent I, then centrifuged at 3500 rpm for 10 min. The supernatant was used directly for the GSH assay, using the kits purchased from Jiancheng (Nanjing, China).

Detection of intracellular lipid peroxidation (LPO)

LPS-treated RAW 264.7 cells were harvested by scraping in isotonic PBS or by trypsinization, then washed at 1000 rpm for 10 min. The cell pellet was resuspended in 0.2–0.3 mL of 0.1 M (pH 7–7.4) phosphate buffer or normal saline and disrupted via ultrasonication (300 W, 3–5 s each, repeated 3–5 times on ice) or manual homogenization. Alternatively, cells were lysed with 1–2% Triton X-100 for 30–40 min. The resulting homogenate or lysate was used directly for the LPO assay, using the kits purchased from Jiancheng (Nanjing, China).

Live/dead staining

For live/dead staining, RAW 264.7 cells were cultured in 24-well plates overnight. Following a 24-h treatment with PPy-Fe NPs, PPy-Fe-MTX NPs, or PPy-FePi-MTX NPs, the cells were rinsed thrice with PBS. The cells were subsequently stained with a Live/Dead Cell Staining Kit (Beyotime Biotechnology) following the manufacturer's instructions. Calcein-AM was utilized to label viable cells, leading to the production of green fluorescence, whereas PI was used to label non-viable cells, resulting in the emission of red fluorescence. The labeled cells were visualized and captured by an inverted Olympus microscope.

Cell viability test

RAW 264.7 was incubated with various concentrations of MTX, PPy-Fe NPs, PPy-Fe-MTX NPs, or PPy-FePi-MTX NPs (0, 50, 100, 200, 400 ppm) for 24 h in the presence or absence of lipopolysaccharide (LPS). Following this, the Cell Counting Kit-8 (CCK-8, Beyotime Biotechnology) assay was used to test cell viability according to the manufacturer's protocol.

Western blot analysis and quantitative reverse transcription polymerase chain reaction (qRT-PCR)

For Western blotting, protein levels were quantified using a bicinchoninic acid (BCA) assay kit (Thermo Fisher Scientific). A total of 40 μg of protein was resolved by SDS-PAGE, transferred onto a PVDF membrane, and blocked. These membranes were then incubated with primary antibodies targeting p53 (1:1500, Proteintech), Beclin-1 (1:1000, Proteintech), p62 (1:1000, Proteintech), Caspase 3 (1:1000, Proteintech), BAX (1:1000, Proteintech), GPX4 (1:1000, Proteintech), and β-actin (1:10000, Fudebio, Hangzhou, China). Following this, HRP-conjugated secondary antibodies (Fudebio, Hangzhou, China) were applied. Detection of the protein bands was achieved using an ECL Kit (Fudebio, Hangzhou, China) and visualized with a gel imaging system (Tanon-5200CE).

Total RNA and protein samples were isolated from RAW 264.7 cells post-treatment using RNAiso Plus (TAKARA) and cell lysis buffer (Cell Signaling Technology), respectively, adhering to the protocols provided by the manufacturers. RNA (1000 ng) was reverse transcribed into cDNA with the First Strand cDNA Synthesis Kit (Thermo Fisher Scientific). Quantitative RT-PCR was then carried out using SYBR Green PCR Master Mix (Thermo Fisher Scientific) on a CFX96 Connect Real-Time PCR Detection System (BIO-RAD).

Histopathological examination

Mouse knee joints were collected, preserved in 4% paraformaldehyde, and decalcified with 15% tetrasodium ethylenediaminetetraacetic acid for 1 month. Section (3 μm thick) were prepared by paraffin embedding and stained with hematoxylin-eosin (H&E), Safranin-O Fast-Green, and tartrate-resistant acid phosphatase (TRAP). The images were visualized and captured by an Olympus microscope.

Immunohistochemical (IHC) staining

Section (3 μm thick) of mou knee joints were subjected to IHC staining with primary antibodies against Nos2, Cd86, GPX4, and p62 (1:100, Proteintech) following standard protocols, and visualized using an Olympus microscope. Quantitative analysis of stained sections was performed using ImageJ software.

Micro-computed tomography (Micro-CT) imaging

The preserved mouse joint samples were scanned with a micro-CT (Inveon Micro-CT, Siemens, Germany) at a resolution of 19 μm using 80-KV voltage, 500-μA current, and 300-ms exposure time. Micro-CT images were examined with Materialise Mimics software (V21.0, Materialise Belgium).

Statistical analysis

Quantitative data were expressed as mean ± standard deviation. Statistical comparisons between two groups were conducted using a Student's two-sided t-test, while multiple group comparisons were performed using one-way analysis of variance (ANOVA). Statistical significance was set at a P-value < 0.05.

Results and discussion

Preparation and characterization of PPy-FePi-MTX NPs

The PPy-FePi-MTX NPs were fabricated through a facile process without organic solvents or harsh reaction temperature (Scheme 1). The transmission electron microscopy (TEM) images (Fig. 1a) show that these particles were well dispersed. Then, the presence of FePi on PPy-FePi-MTX NPs was detected in high-angle annular dark field (HAADF) image (Fig. 1b). As shown in Fig. 1c-e, the hydrodynamic dimensions of the prepared PPy-Fe NPs, PPy-Fe-MTX NPs, and PPy-FePi-MTX NPs were 153.0 nm, 165.3 nm and 177.0 nm, respectively. The zeta potential of PPy-FePi-MTX NPs was – 1.2 mV (Fig. 1f). Compared to the UV-Vis spectra of PPy-Fe, PPy-FePi-MTX showed the characteristic absorption peak of MTX at 300 nm, which confirmed the successful loading of MTX (Fig. 1g). The loading contents of MTX and Fe were calculated to be 9.98% by UV-Vis measurement and 0.51% by inductively coupled plasma optical emission spectrometry (ICP-OES) measurement, respectively. The amorphous structure of PPy-FePi-MTX NPs was revealed by X-ray diffraction (XRD) analysis (Fig. 1h). The coexistence of Fe, P, and O was demonstrated by X-ray photoelectron spectroscopy (XPS) analysis (Fig. S1). As shown in the high-resolution XPS spectra of Fe, the peaks located at 709.9 and 723.4 eV corresponded to the Fe 2p 3/2 (Fe^{2+}) and Fe 2p 1/2 (Fe^{3+}) signals, respectively, proving the multivalence of iron ions in PPy-FePi-MTX NPs (Fig. 1i).

Under NIR laser irradiation, the photothermal stability of PPy-FePi-MTX NPs was investigated. During four heating-cooling cycles, the temperature curve displayed good reproducibility, proving the desirable photothermal stability of PPy-FePi-MTX NPs (Fig. 2a). The solution temperature of PPy-FePi-MTX NPs was found to show positive correlation with laser irradiation time and NP concentration (Fig. 2b-c). Based on a previously reported well-established method [40], the photothermal conversion efficiency of PPy-FePi-MTX NPs was calculated to be 28.7% (Fig. 2d-e). Subsequently, the release behavior of MTX from PPy-FePi-MTX NPs was explored under different temperature conditions (Fig. 2f). It can be seen that the released amount of MTX increased with time and temperature. The photothermal effect of PPy was expected to accelerate the release of MTX under laser irradiation, showing synergistic effect.

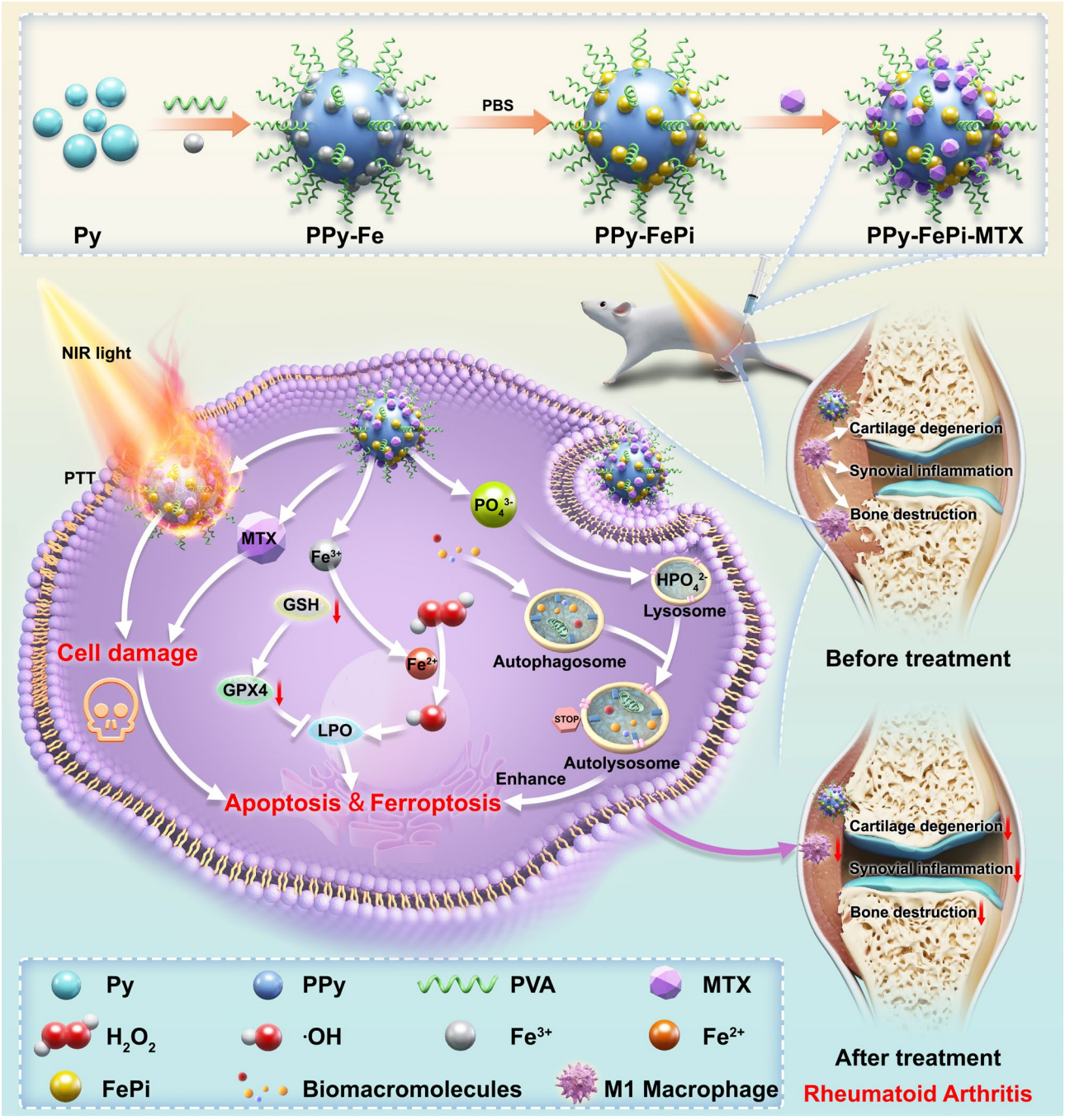

Scheme 1 Schematic illustration of the synthesis process and therapeutic mechanism of PPy-FePi-MTX NPs for RA treatment. The final PPy-FePi-MTX NPs were prepared through the polymerization of pyrrole monomer, the formation of FePi NPs, and the loading MTX. The NPs are designed to release their payloads in response to the inflammatory microenvironment. MTX and PPy under NIR irradiation synergistically induce apoptosis in M1 macrophages. Simultaneously, Fe^{3+} react with GSH to produce Fe^{2+}, which catalyze the conversion of H_2O_2 into cytotoxic ·OH. This process leads to the depletion of GSH, inactivation of GPX4, and initiation of lipid peroxidation-driven ferroptosis. Additionally, PO_4^{3-} further disrupt lysosomal pH, thereby inhibiting cytoprotective autophagy and enhancing the therapeutic efficacy against RA.

The GSH depletion capacity of PPy-FePi-MTX NPs was investigated using DTNB as the probe (Fig. 2g). The data showed that GSH level decreased with the increasing concentration of PPy-FePi-MTX NPs, proving good GSH consumption ability and indicating the generation of Fe^{2+} after this reaction. Then, the production of ·OH through Fe^{2+}-mediated Fenton reaction was detected using MB as the probe. As shown in Fig. 2h, the MB peak gradually decreases with the increase of nanoparticle concentration, indicating the production of ·OH.

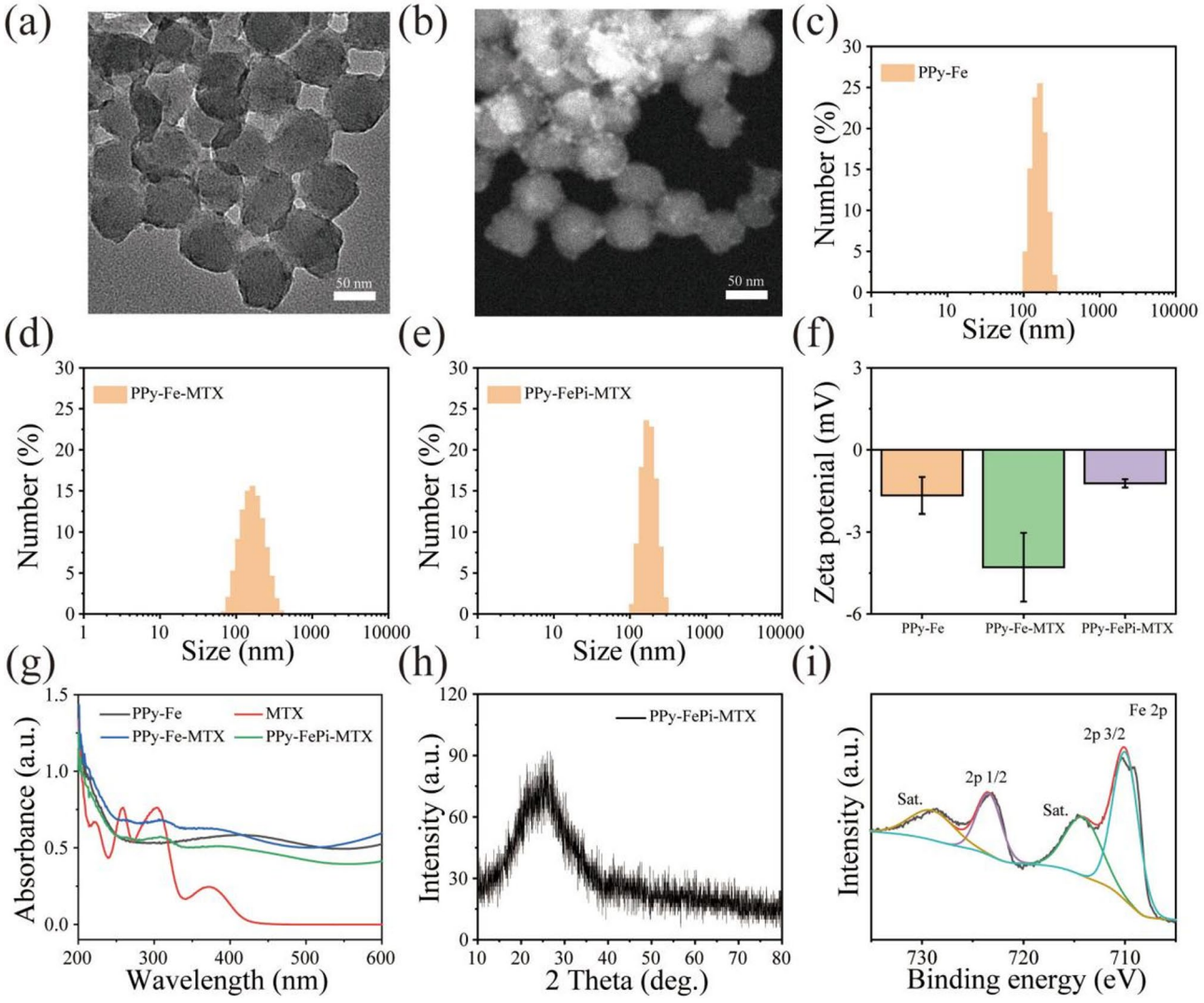

Fig. 1 Characterization of the formed PPy-FePi-MTX NPs. (**a**) TEM image and (**b**) HAADF image of PPy-FePi-MTX NPs. Hydrodynamic size distribution of (**c**) PPy-Fe NPs, (**d**) PPy-Fe-MTX NPs, and (**e**) PPy-FePi-MTX NPs. (**f**) Zeta potential data of PPy-Fe NPs, PPy-Fe-MTX NPs, and PPy-FePi-MTX NPs in an aqueous solution. (**g**) UV-Vis absorption spectra of PPy-Fe NPs, MTX, PPy-Fe-MTX NPs, and PPy-FePi-MTX NPs. (**h**) XRD pattern of PPy-FePi-MTX NPs. (**i**) The high-resolution XPS spectrum of Fe 2p for PPy-FePi-MTX NPs

In vitro cellular uptake and cytotoxicity assay

Subsequently, the internalization of PPy-FePi-MTX NPs by murine RAW 264.7 cells was investigated through a confocal laser scanning microscope (CLSM). These NPs were fluorescently labeled with 5-FAM for tracking their intracellular localization within cells, and DAPI was used to visualize the nuclei. RAW 264.7 cells were exposed to PPy-FePi-MTX NPs for varying durations of 0, 2, 4, and 6 h. CLSM images demonstrated significant cellular uptake of PPy-FePi-MTX NPs by macrophages, with the extent of internalization dependent on both the duration of exposure and the concentration of nanoparticles (Fig. S2). With increased incubation time, there was a corresponding elevation in the uptake of PPy-FePi-MTX NPs, leading to enhanced intracellular green fluorescence, which is primarily localized within the cytoplasm, with the absence of green fluorescence in the nucleus. The green fluorescence emitted by PPy-FePi-MTX NPs predominantly co-localized with endosomes/lysosomes after 2 h of culture. Upon extending the culture time to 4 and 6 h, the PPy-FePi-MTX NPs were exclusively localized within cytoplasm, as evidenced by a distinct segregation of the green and red fluorescence signals (Fig. 3a). This revealed that PPy-FePi-MTX NPs internalized by RAW 264.7 cells underwent a gradual translocation from endosomes/lysosomes to the cytoplasm, suggesting a process of endosomal escape. Moreover, high-magnification CLSM images provided evidence of this translocation and confirmed the endosomal escape of PPy-FePi-MTX NPs, as indicated in Fig. S3. The fluorescence intensity

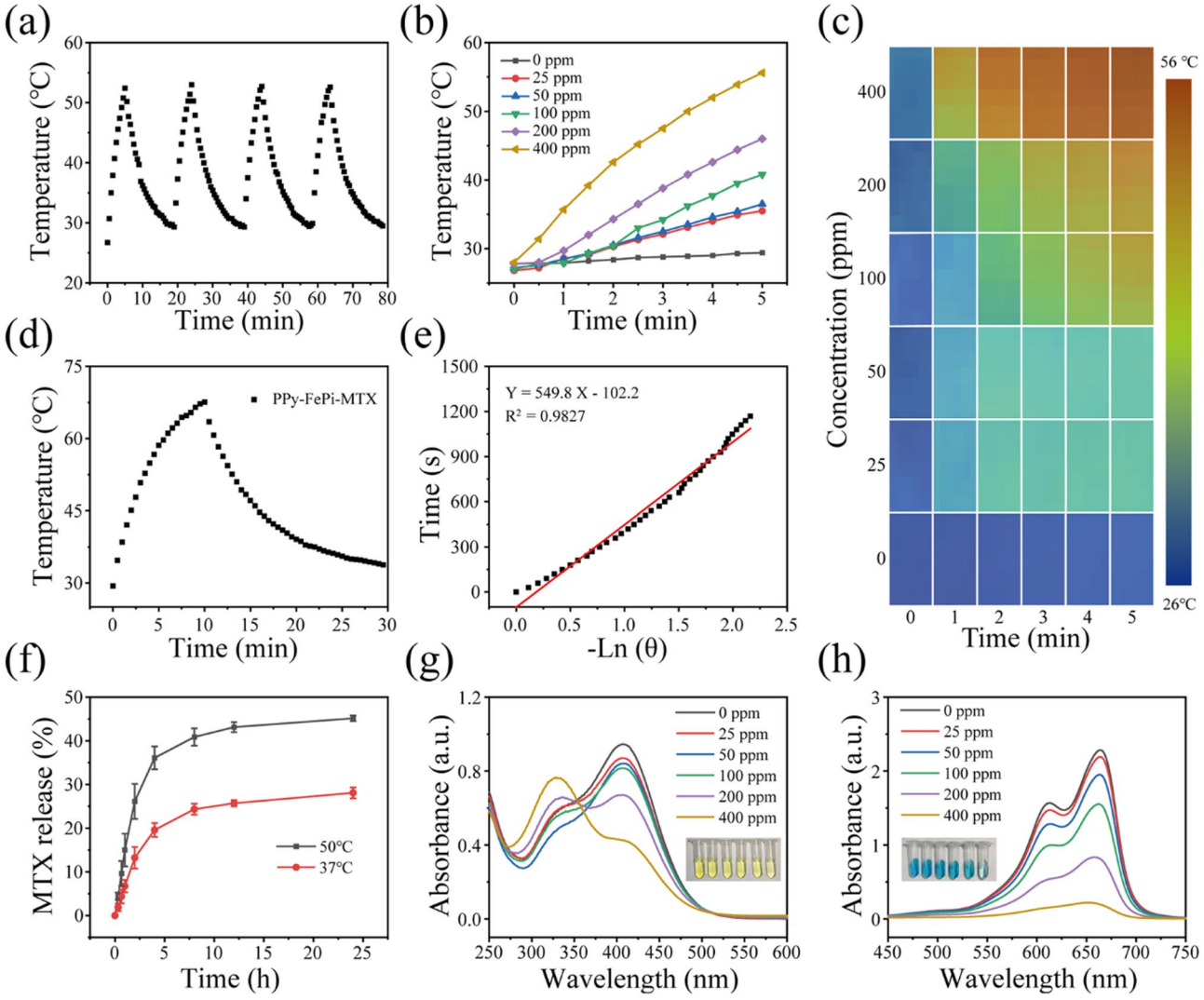

Fig. 2 Performance evaluation of the formed PPy-FePi-MTX NPs. (**a**) Temperature curve of PPy-FePi-MTX NPs during four heating-cooling cycles under laser irradiation (1064 nm, 1.0 W/cm^2). (**b**) Temperature curves and (**c**) thermal images of PPy-FePi-MTX NPs with different concentrations under the same laser irradiation. (**d**) Heating-cooling curve and (**e**) time constant fitting curve of PPy-FePi-MTX NPs under laser irradiation for 10 min and cool down for 20 min. (**f**) MTX release curves from PPy-FePi-MTX NPs at different temperatures. (**g**) UV-Vis spectra for GSH detection using DTNB as the probe when incubated with PPy-FePi-MTX NPs. (**h**) UV-Vis spectra for ·OH detection using MB as the probe when incubated with PPy-FePi-MTX NPs

analysis indicated the stability of lysosomal labeling and the increasing uptake of NPs with longer incubation durations (Fig. 3b).

The cytotoxic effects of different NPs on RAW 264.7 cells were assessed by CCK-8 assay. Following 24 h incubation, these various NPs did not exhibit obvious cytotoxic effects at concentrations up to 200 ppm. When incubation with 400 ppm PPy-Fe NPs, PPy-Fe-MTX NPs, or PPy-FePi-MTX NPs, the viability of RAW 264.7 cells reduced to 88.69%, 83.15%, and 80.15%, respectively (Fig. 3c). The results of Calcein-AM and propidium iodide (AM/PI) staining also showed that 50, 100, or 200 ppm PPy-FePi-MTX NPs did not demonstrate cytotoxic effects after 24 h of incubation, with mild cytotoxicity observed at a concentration of 400 ppm (Fig. 3d-e). These findings indicated the desirable cytocompatibility of these NPs with normal macrophages at concentrations below 200 ppm. Following exposure to lipopolysaccharide (LPS) at a concentration of 200 ppm in various treatments, the survival rate of pro-inflammatory M1 macrophages in the MTX group was 76.69%. This rate was 80.64%, 60.48%, and 35.16% in the PPy-Fe, PPy-Fe-MTX, and PPy-FePi-MTX groups, respectively (Fig. 3f). These results indicated that the therapeutic efficacy of PPy-FePi-MTX NPs exhibited specificity towards inflammatory macrophages, potentially due to variations in the intracellular microenvironment between normal and inflammatory macrophages [41]. The observed selectivity supported the good biosafety of PPy-FePi-MTX NPs.

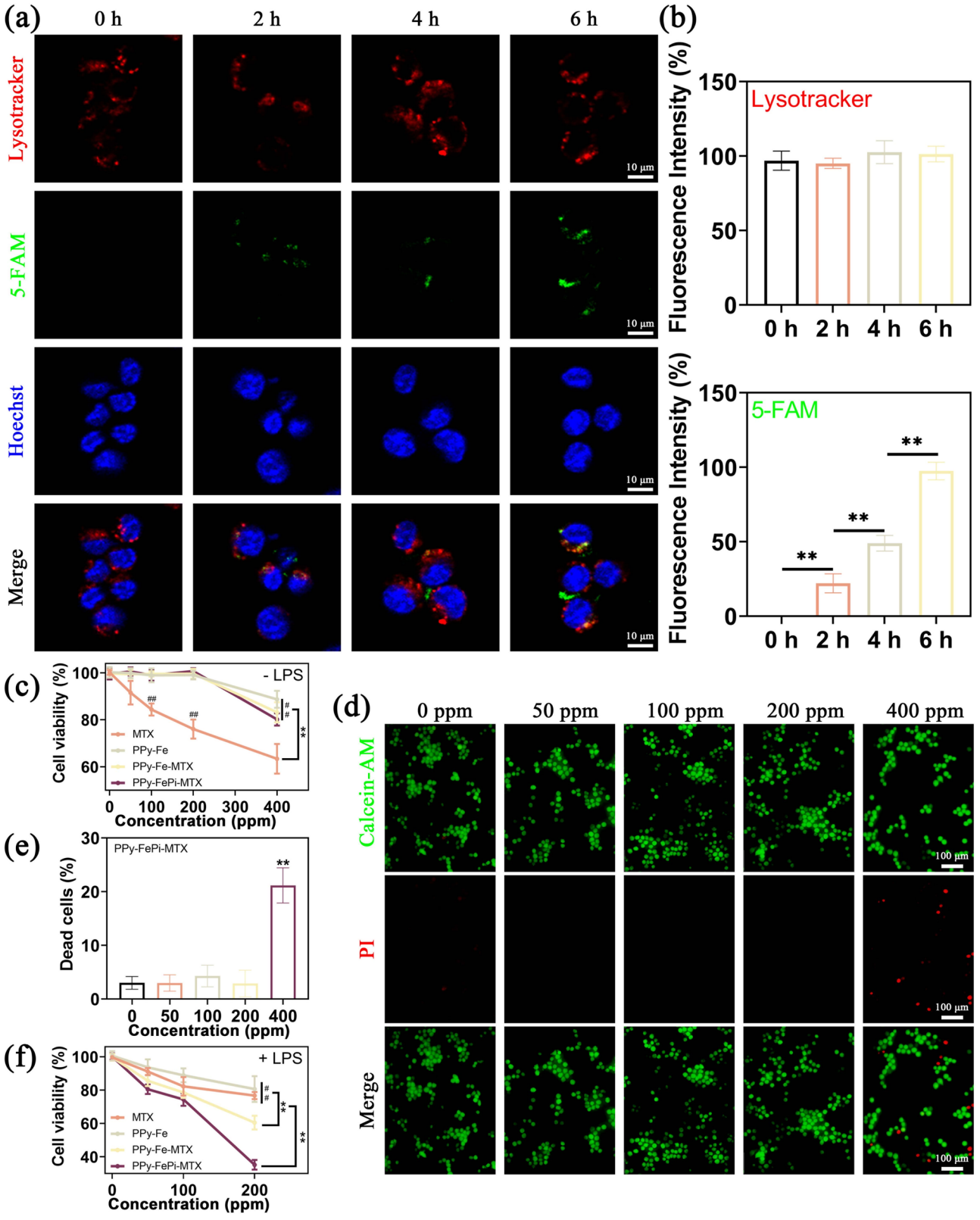

Fig. 3 (See legend on next page.)

(See figure on previous page.)

Fig. 3 Analysis of cellular uptake, cell viability, and cytotoxicity. (a, b) CLSM images (**a**) and quantitative analysis (**b**) of cells incubated with 5-FAM-labelled PPy-FePi-MTX NPs. The lysosomes, PPy-FePi-MTX NPs, and nuclei were marked in red, green, and blue, respectively. Scale bar: 10 μm. (**c**) Cell viability assessed with different concentrations of MTX, PPy-Fe, PPy-Fe-MTX, and PPy-FePi-MTX NPs without LPS. (**d**, **e**) Live/dead staining images and quantification after treatment with different concentrations of PPy-FePi-MTX NPs without LPS. Calcein-AM (green) indicated live cells, and PI (red) indicated dead cells. Scale bar: 100 μm. (**f**) Cell viability assessed with different concentrations of MTX, PPy-Fe, PPy-Fe-MTX, and PPy-FePi-MTX with LPS. # indicate significant differences in comparison to PBS group. $^{\#\#}$, $^{**}p < 0.01$

Apoptosis and ferroptosis mechanism analysis

With good cytocompatibility, the PPy-FePi-MTX NPs were further evaluated with an in-depth investigation into the therapeutic mechanisms associated with the apoptosis and ferroptosis of inflammatory macrophages at a concentration of 200 ppm. As illustrated in Scheme 1, the degradation of PPy-FePi-MTX NPs occurred upon uptaken by inflammatory macrophages, resulting in the release of Fe^{3+} and MTX. The liberated MTX was capable of inducing apoptosis and inhibiting proliferation directly. Furthermore, Fe^{3+} can be converted to Fe^{2+} through a redox reaction with GSH. The resultant Fe^{2+} then catalyzed the conversion of H_2O_2 to ·OH, leading to intracellular oxidative stress. As a consequence of GSH depletion, GPX4 became inactivated, compromising the oxidative defense mechanism of inflammatory cells. Consequently, the combined effects of apoptosis and ferroptosis induced by PPy-FePi-MTX NPs contributed to the elimination of inflammatory cells.

To evaluate the apoptosis-inducing capacity of PPy-FePi-MTX NPs, LPS-treated RAW 264.7 cells were divided into 5 groups with or without 1064 nm irradiation: (1) PBS, (2) MTX, (3) PPy-Fe NPs, (4) PPy-Fe-MTX NPs, and (5) PPy-FePi-MTX NPs. The findings from the AM/PI staining and CCK-8 assay revealed that treatment with MTX or PPy-Fe NPs, in the absence of irradiation, led to decreased cell viability in comparison to the PBS group. The PPy-Fe-MTX NPs groups without irradiation exhibited a higher cytotoxic effect when compared to equivalent concentrations of MTX or PPy-Fe NPs without irradiation (Fig. S4). Following irradiation treatment, the efficacy of PPy-Fe NPs, PPy-Fe-MTX NPs, and PPy-FePi-MTX NPs to kill LPS-treated RAW 264.7 cells was significantly enhanced (Table S2). Notably, a pronounced reduction of the cell viability was observed in the PPy-FePi-MTX group compared to the PPy-Fe-MTX group, indicating PO_4^{3-}-mediated autophagy blockage could effectively enhance the inflammatory cell-eliminating capacity of PPy-Fe-MTX NPs (Fig. 4a-c). These results suggested the combined therapeutic effects generated by PPy-FePi-MTX NPs was more effective in causing macrophage damage.

To further demonstrate the combined effects of photothermal therapy and MTX release from PPy-FePi-MTX NPs, after staining LPS-treated RAW 264.7 cells with Annexin V-FITC and PI, apoptosis levels were quantified by flow cytometry (Fig. 4d). The results showed that the apoptosis rate of cells in the PPy-FePi-MTX NPs group was 91.2%, significantly surpassing that of the other groups. Additionally, results from immunoblot analysis and qRT-PCR identified a striking upregulation in the expression of cleaved Caspase 3 and BAX in the PPy-FePi-MTX NPs group compared to the other groups (Fig. 4e and S5). These results collectively revealed the effectiveness of combined therapeutic strategy.

Subsequently, the capacity of PPy-FePi-MTX NPs to induce ferroptosis was examined. Firstly, the production of ROS was investigated under different conditions using 2',7'-dichlorofluorescein diacetate as the probe. The results depicted in Fig. S6a-b demonstrated that the intensity of green fluorescence heightened with prolonged exposure to irradiation, indicating a gradual escalation in ROS production, reaching its maximum level at 5 min. Compared to the PBS group, obviously increased green fluorescent signals were observed in the other groups, with particularly enhanced brightness noted in the PPy-FePi-MTX group (Fig. S6c-d). These images showed the elevated levels of ROS after PPy-FePi-MTX NPs treatment. Furthermore, 3'-(*p*-aminophenyl) fluorescein (APF) was utilized to confirm the generation of ·OH [11, 42]. The results from APF analysis indicated that the production of ·OH increased as the duration of laser irradiation was extended (Fig. S7a). Similarly, the PPy-FePi-MTX group exhibited a higher production level of ·OH compared to the other groups when subjected to laser irradiation, supporting the elevated generation of ·OH in the PPy-FePi-MTX group (Fig. S7b).

The reduction of GSH by Fe^{3+} was evaluated in LPS-treated RAW 264.7 cells (Fig. 4f). Following co-incubation with PPy-FePi-MTX NPs, a significant decrease in intracellular GSH levels was observed, indicating GSH depletion and subsequent disruption of intracellular processes as confirmed by immunoblotting assay (Fig. 4e and g). The striking downregulation of GPX4 expression in the PPy-FePi-MTX NPs group suggested effective GSH depletion leading to GPX4 inactivation. Furthermore, the LPO level within cells was found to be crucial to this process [21]. The PPy-FePi-MTX NPs group exhibited an obvious increase in the LPO content, indicating the induction of ferroptosis (Fig. 4h). Collectively, these findings revealed that the synthesized PPy-FePi-MTX NPs effectively triggered apoptosis and ferroptosis in inflammatory macrophages.

Autophagy blockage analysis

Autophagy serves as a cytoprotective mechanism by facilitating the digestion of toxic proteins and damaged organelles through lysosomes (Scheme 1) [23, 43]. Additionally, the nutrients obtained from autophagic degradation, such as amino acids and pyruvate, play a crucial role in supporting mitochondrial metabolism and the biosynthesis of inflammatory macrophages, thereby enhancing their viability. Consequently, the inhibition of autophagy process is essential for the suppression of inflammation. During the degradation process of PPy-FePi-MTX NPs, a significant amount of PO_4^{3-} was released within inflammatory macrophages. The accumulation of PO_4^{3-} in the lysosome led to hydrolase inactivation due to the disruption of optimal reaction pH [44, 45], thereby impeding the metabolism of damaged components and ultimately resulting in the death of inflammatory macrophages.

We systematically investigated the ability of PPy-FePi-MTX NPs to inhibit autophagy. The effects of MTX, PPy-Fe NPs, PPy-Fe-MTX NPs, and PPy-FePi-MTX NPs on autophagic flux were examined to understand the relationship between cellular self-repair and autophagy. The autophagy-related protein LC3B was utilized as a marker. LPS-treated RAW 264.7 cells were transfected with LC3B pcDNA tagged with green fluorescent protein (GFP) and subsequently treated with MTX, PPy-Fe NPs, PPy-Fe-MTX NPs, or PPy-FePi-MTX NPs. Conspicuous green fluorescence emitted by GFP-LC3B was observed in the PPy-FePi-MTX group, indicating the formation of autophagosomes (Fig. 5a-c). These data could be attributed to the activation of effective autophagy or the inhibition of lysosomal degradation.

Additional molecular evidence was necessary to elucidate this phenomenon. Immunoblotting and qRT-PCR analyses were conducted on LPS-treated RAW 264.7 cells to assess the expression of autophagy-related genes (Fig. 5d-g). The protein and mRNA expression of p53, functioning as a transcriptional sensor of ROS [46], were progressively increased in the MTX, PPy-Fe, PPy-Fe-MTX, and PPy-FePi-MTX groups. This suggested that the cellular redox state played a significant role in modulating downstream autophagic responses. The gradually upregulated protein and mRNA expression of Beclin-1, an important regulator of the initial stages of autophagy and the formation of phagophores [47], was observed in the MTX, PPy-Fe, PPy-Fe-MTX, and PPy-FePi-MTX groups. This observation indicated that the therapeutic interventions induced a protective autophagy aimed at mitigating cellular damage. Importantly, the accumulation of p62, a specific substrate targeted to the autophagosomal membrane for degradation in autolysosomes [48], was observed in the PPy-FePi-MTX group, indicating inhibition of lysosomal degradation. Conversely, a significant downregulation of p62 in the MTX, PPy-Fe, and PPy-Fe-MTX groups further demonstrated that these treatments effectively induced protective autophagy. These findings offered robust supporting evidence for distinguishing positive and negative regulation of autophagy. The PPy-FePi-MTX NPs exhibited dual effects by inducing damage to enhance autolysosome processing and inhibiting autolysosome degradation to accumulate autophagy substrates. Our data on apoptosis and ferroptosis collectively indicated that the phosphate-triggered blockade of autophagy hindered the self-repair capability of inflammatory macrophages during the process of apoptosis/ferroptosis-induced destruction, thereby enhancing anti-inflammatory therapeutic efficacy [49, 50].

Therapeutic efficacy detection in vivo

In order to investigate the photothermal capability of PPy-FePi-MTX NPs to treat RA, a CIA-induced mouse RA mouse model was subjected to the therapeutic procedure as illustrated in Fig. 6a. The mice were immunized on Day 0, and CIA was established by Day 21. From Day 21 onwards, the RA mice were treated with different therapeutics every 7 d. The evaluation was performed every 3 days, and the mice were sacrificed for tissue collection on Day 60. It was found that under 1064 nm laser irradiation, the sham and vehicle groups exhibited the weakest photothermal effects due to the absence of a photothermal agent. In contrast, the PPy-Fe, PPy-FeMTX, and PPy-Fe-MTX groups demonstrated similar photothermal effects, reaching temperatures of approximately 48 °C under laser irradiation. No photothermal effect was observed in PPy-FePi-MTX groups without laser irradiation (Fig. 6b).

To evaluate the anti-RA effect of PPy-FePi-MTX NPs, MTX, a frequently used small-molecule disease-modifying antirheumatic drug [51], was utilized as the positive control group. Using a clinical rating system [52], arthritis severity, paw thickness, and joint diameter were assessed. Compared to the vehicle plus laser group, a mild improvement of arthritis index was found in the PPy-Fe NPs plus laser group, which was less effective than the MTX group. In contrast, the PPy-FePi-MTX plus laser group significantly improved arthritis index compared to other groups, showing the lowest arthritis index (Fig. 7a). Meanwhile, PPy-FePi-MTX NPs-treated mice under laser irradiation showed an obvious decrease in paw thickness and joint swelling (Fig. 7b-d). Compared to previously reported methods [53–55], our findings indicated the high effectiveness of this anti-RA treatment strategy through autophagy blockage-enhanced apoptosis/ferroptosis.

To assess the degree of joint inflammation more comprehensively, a histological analysis of joint slides from mice was conducted. Examination of H&E-stained

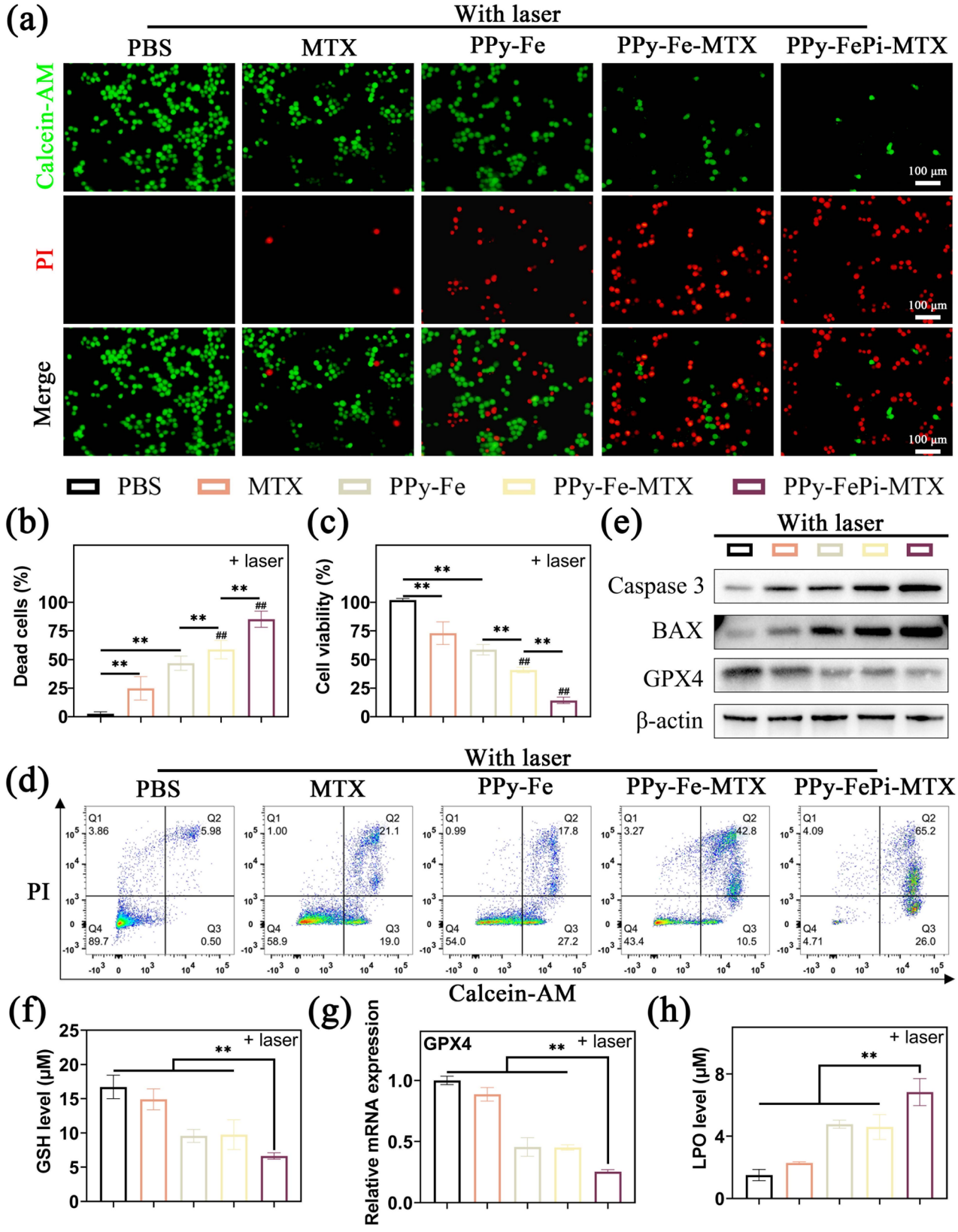

Fig. 4 Cytotoxic effects and apoptosis/ferroptosis analysis in LPS-treated RAW 264.7 cells with different treatments under laser irradiation. (**a**, **b**) CLSM images (a) and quantitative analysis (**b**) of live/dead cell staining images. Scale bar: 100 μm. (**c**) Quantification of cell viability. (**d**) Flow cytometry analysis of cellular apoptosis. (**e**) Western blot analysis of Caspase 3, BAX, and GPX4 proteins expression. (**f**, **h**) Measurement of intracellular (**f**) GSH and (h) LPO levels. (**g**) RT-qPCR analysis of GPX4 mRNA expression. # indicate significant differences in comparison to PBS group. $^{\#,}$ $^{*}p < 0.05$, $^{**}p < 0.01$

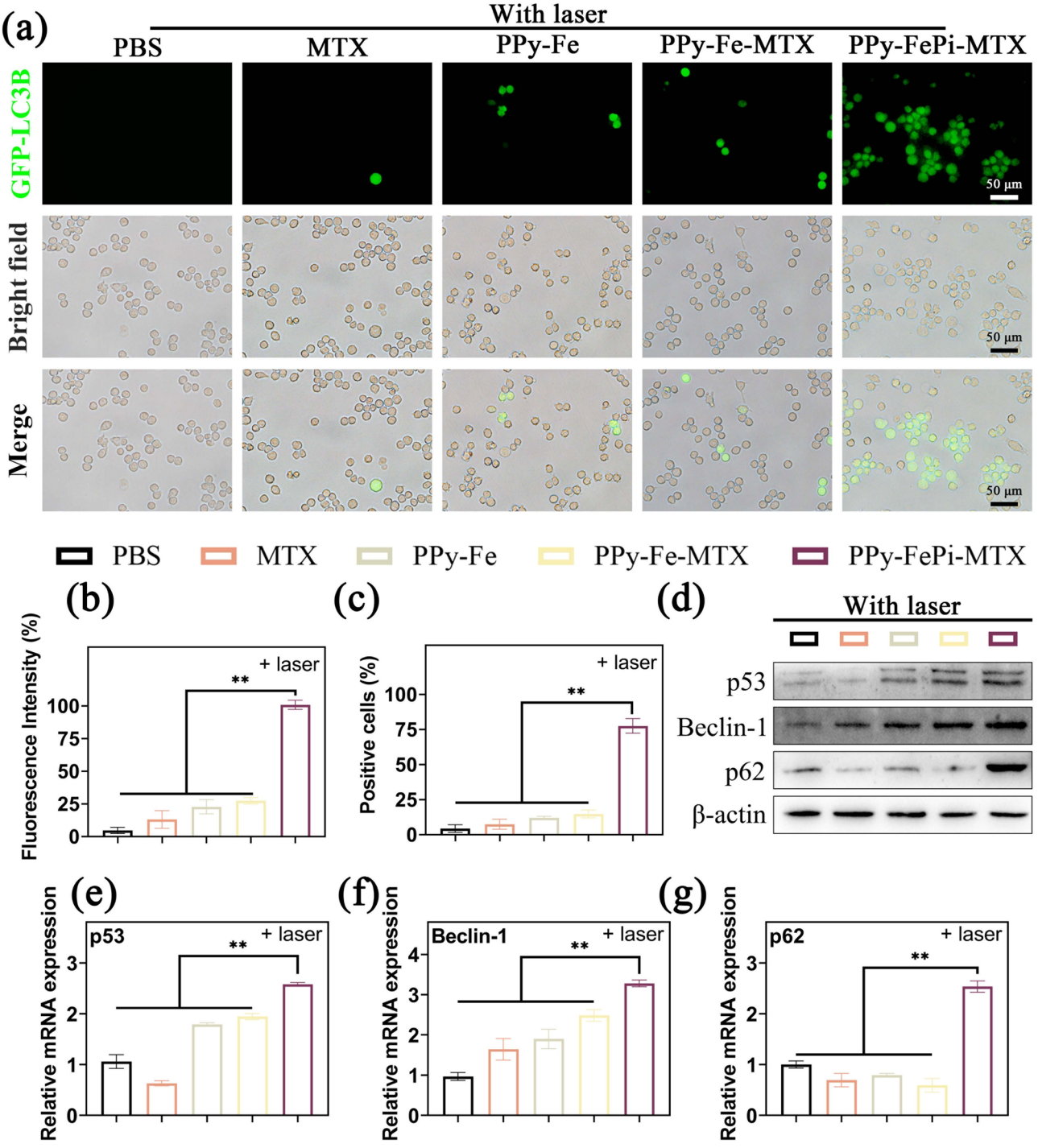

Fig. 5 Analysis of autophagy and protein/mRNA expression in LPS-treated RAW 264.7 cells with various treatments under laser irradiation. (**a**-**c**) GFP-LC3B (green) fluorescence images (**a**), quantitative analysis (**b**), and positive cell percentages (**c**). Scale bar: 50 μm. (**d**) Western blot analysis of p53, Beclin-1, and p62 proteins expression. (e-g) RT-qPCR analysis of p53 (**e**), Beclin-1 (**f**), and p62 (**g**) mRNA expression. $^{**}p < 0.01$

sections in PBS-treated CIA mice revealed the presence of significant inflammatory cell infiltration and pronounced synovial hyperplasia. In comparison to the PBS plus laser group, the MTX, PPy-Fe plus laser, PPy-Fe-MTX plus laser, and PPy-FePi-MTX without laser group demonstrated limited efficacy in mitigating these symptoms. Conversely, the PPy-FePi-MTX plus laser group showed the optimal effect in reducing synovial hyperplasia and inflammation, as well as a significantly decreased synovitis score (Fig. 8a and e). The in vivo serum levels of proinflammatory cytokines (TNF-α, IL-1β, and IL-6) were also assessed following various

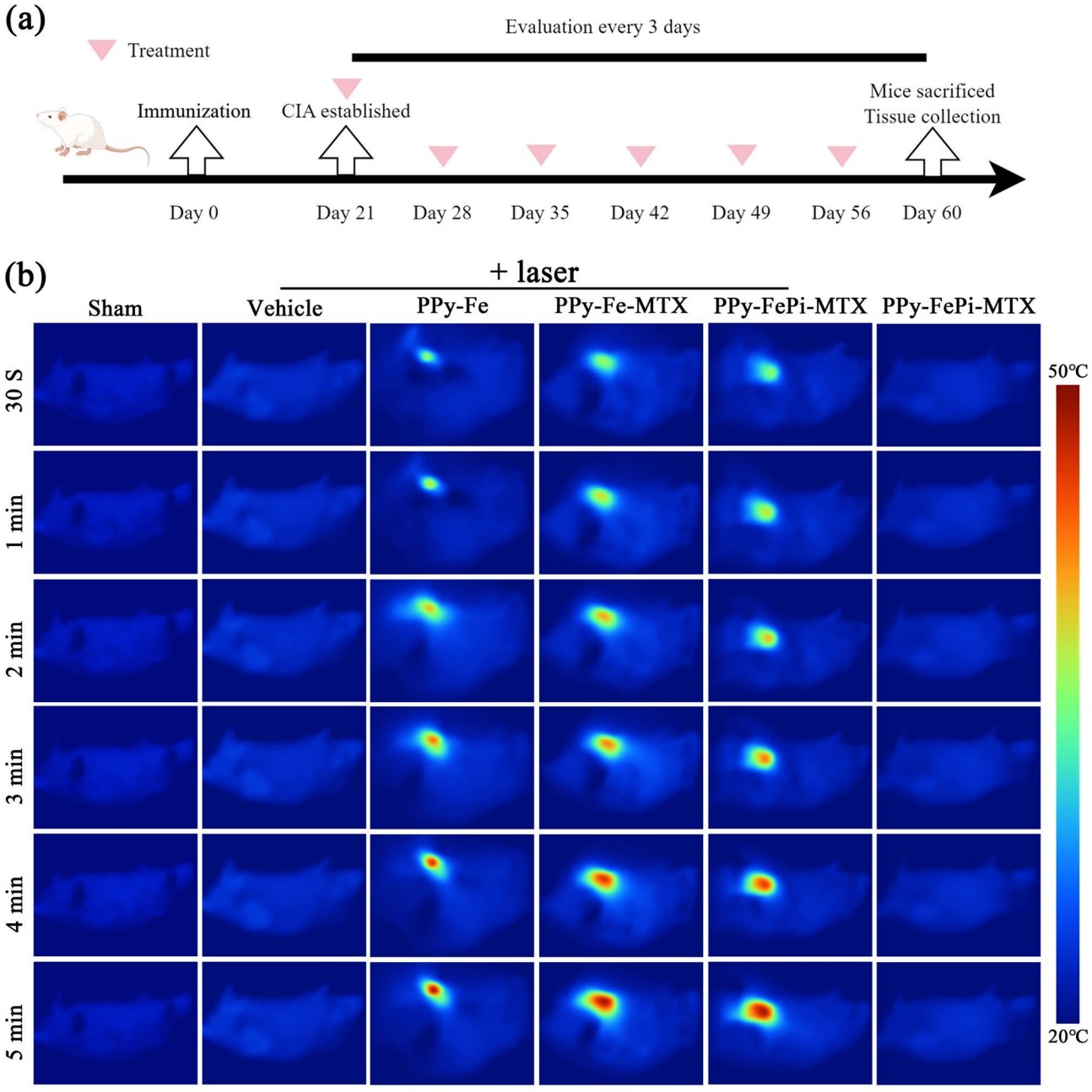

Fig. 6 Evaluation of photothermal effects in a CIA mouse model treated with different NPs or vehicle. (**a**) Schematic representation of the experimental timeline. This figure was created using Figdraw (www.figdraw.com). (**b**) Infrared thermal imaging of mice with various treatments under laser irradiation (+ laser) at various time points

treatments as an additional critical parameter for evaluating therapeutic efficacy. Notably, significantly reduced levels of TNF-α, IL-1β, and IL-6 were observed in groups 3–7, with group 7 demonstrating the most pronounced effect in suppressing proinflammatory cytokines (Fig. S9). These data demonstrated the superiority of combined treatment. Moreover, results from immunohistochemistry (IHC) staining indicated a marked increase in M1 marker, such as Cd86 and Nos2 [56], within the synovium of CIA mice in comparison to the sham group. In contrast, the expression of Cd86 and Nos2 in synovial tissue was substantially reduced in the MTX, PPy-Fe plus laser, PPy-Fe-MTX plus laser, PPy-FePi-MTX plus laser, and PPy-FePi-MTX without laser group. Among these groups, the lowest expression of Cd86 (Fig. 9a and e) and Nos2 (Fig. 9b and f) were observed in the PPy-FePi-MTX plus laser group, which suggested PPy-FePi-MTX NPs effectively eliminated M1-polarized macrophages to alleviate synovial inflammation.

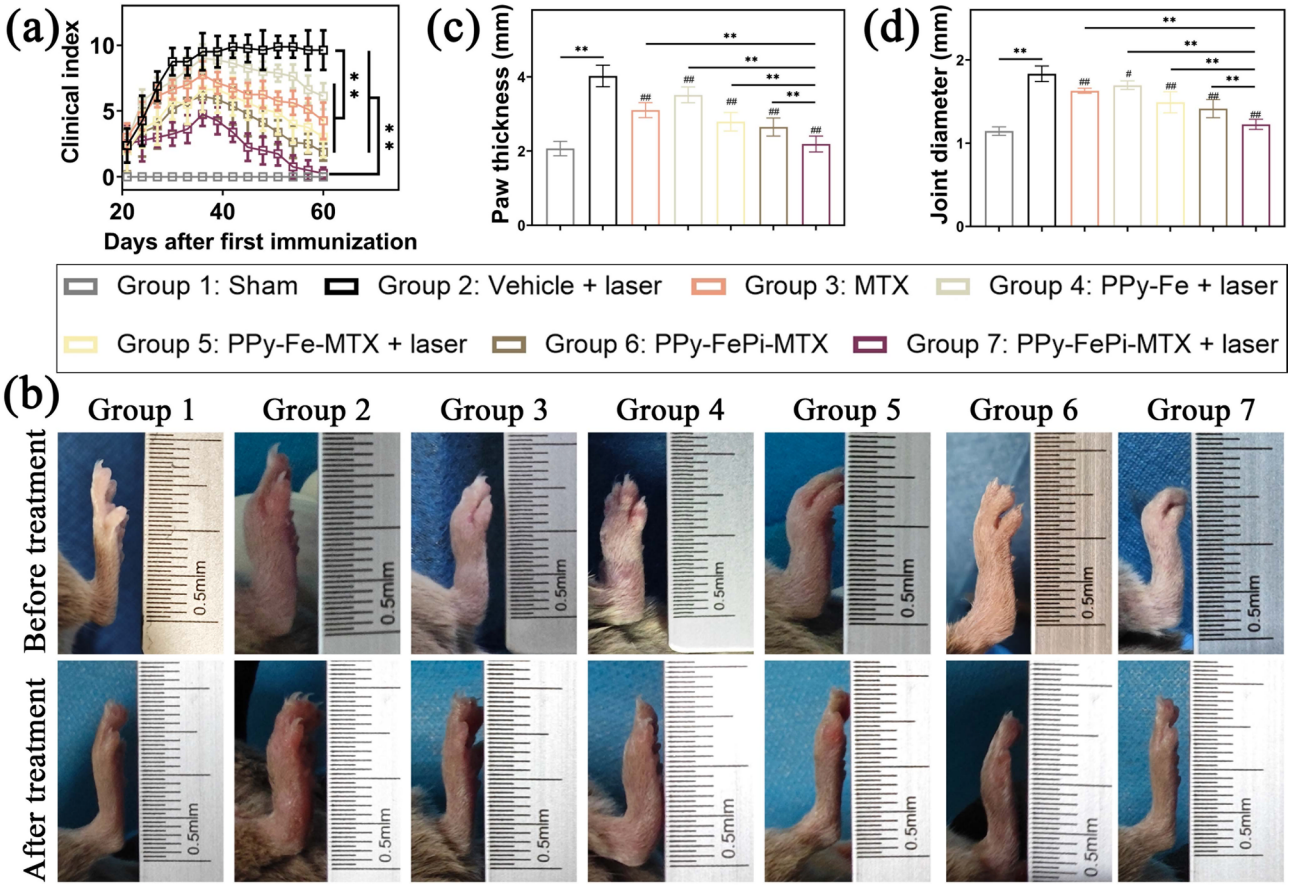

Fig. 7 Evaluation of therapeutic effects on CIA mice based on paw thickness and joint diameter. (**a**) Time course of clinical index of arthritis in different treatment groups over 60 d. (**b**) Representative images of mouse paws before and after treatment in seven different groups. The images included a scale to measure paw thickness and joint diameter. Statistical analysis of (**c**) paw thickness and (**d**) joint diameter on Day 60. # indicate significant differences in comparison to group 2. $^{\#}p < 0.05$, $^{\#\#,**}p < 0.01$

In order to further validate the therapeutic mechanism, IHC was performed to assess the expression of GPX4 (Fig. 9c and g) and p62 (Fig. 9d and h) in synovial tissues. The vehicle plus laser exhibited mildly decreased GPX4 expression, whereas the expression of GPX4 was obviously reduced in the MTX, PPy-Fe plus laser, PPy-Fe-MTX plus laser, PPy-FePi-MTX plus laser, and PPy-FePi-MTX without laser groups. These findings suggested that MTX, PPy-Fe NPs, PPy-Fe-MTX NPs, and PPy-FePi-MTX NPs had the potential to induce ferroptosis effectively for RA treatment. The downregulation of p62 expression in the inflamed synovium from the MTX, PPy-Fe plus laser, and PPy-Fe-MTX plus laser groups, as compared to that of the PBS plus laser group, suggested a potential mechanism by which inflammatory cells might exhibit resistance to treatment and promote self-repair through autophagy. In contrast, the upregulation of p62 expression in the PPy-FePi-MTX with or without laser groups, demonstrated the effective inhibition of autophagy by phosphate. Collectively, these findings illustrated that intracellular intrinsic autophagy can enhance the treatment resistance of inflammatory cells, thereby diminishing therapeutic effectiveness [57]. The suppression of autophagy significantly attenuates this self-protective mechanism, thus enhancing the potential efficacy of nanomedicine.

Chronic synovitis frequently results in cartilage degradation and bone destruction [58]. Histological examination and micro-CT analysis were conducted to evaluate the potential of PPy-FePi-MTX NPs in alleviating inflammatory cartilage and bone degeneration. Safranin-O/Fast-Green staining revealed an obvious destruction of cartilage tissues within the joints of the PBS group. A slight mitigation of cartilage damage was noted in the MTX, PPy-Fe plus laser, PPy-Fe-MTX plus laser, and PPy-FePi-MTX without laser groups. In marked contrast, the joints treated with PPy-FePi-MTX NPs under laser irradiation exhibited intact cartilage (stained red by Safranin O), suggesting the effective protection of articular cartilage (Fig. 8b and f). In micro-CT analysis, various degrees of evident bone damage were observed in the MTX, PPy-Fe plus laser, PPy-Fe-MTX plus laser,

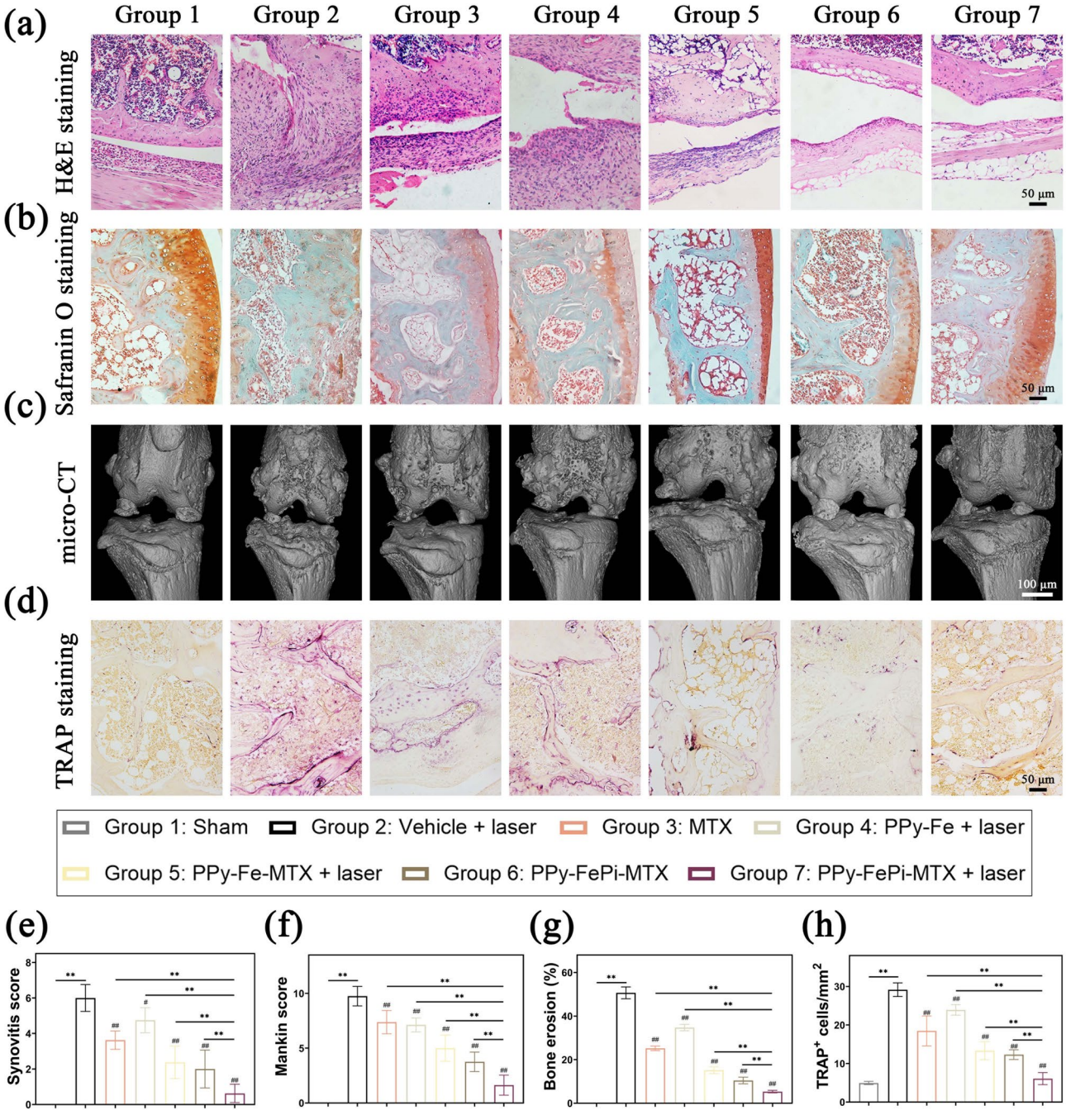

Fig. 8 Histological and micro-CT evaluation of CIA mice after different treatments. (**a**) H&E staining, (**b**) Safranin O staining, (**c**) micro-CT reconstruction images, and (**d**) TRAP staining of joint tissues from various treatment groups. Scale bar: 50 μm and 100 μm. (**e**) Synovitis score based on H&E staining. (**f**) Mankin score based on Safranin O staining. (**g**) Quantification of bone erosion percentage based on micro-CT images. (**h**) Quantification of TRAP-positive cells. # indicate significant differences in comparison to group 2. $^{\#}p < 0.05$, $^{\#\#,**}p < 0.01$

and PPy-FePi-MTX without laser groups. Treatment with PPy-FePi-MTX plus laser exhibited a significant reduction in bone erosion compared to the aforementioned groups (Fig. 8c and g). Increased osteoclasts are known to significantly contribute to bone erosion during the progression of RA [59]. Following this, we conducted an assessment of the effect of PPy-FePi-MTX NPs on osteoclast quantity through tartrate-resistant acid phosphatase (TRAP) staining. Multinuclear cells expressing TRAP and possessing more than three nuclei were characterized as osteoclasts [60]. An obvious increase in osteoclasts was noted in the subchondral bone of the PBS group, while PPy-FePi-MTX NPs under laser treatment led to a marked reduction in the number of osteoclasts

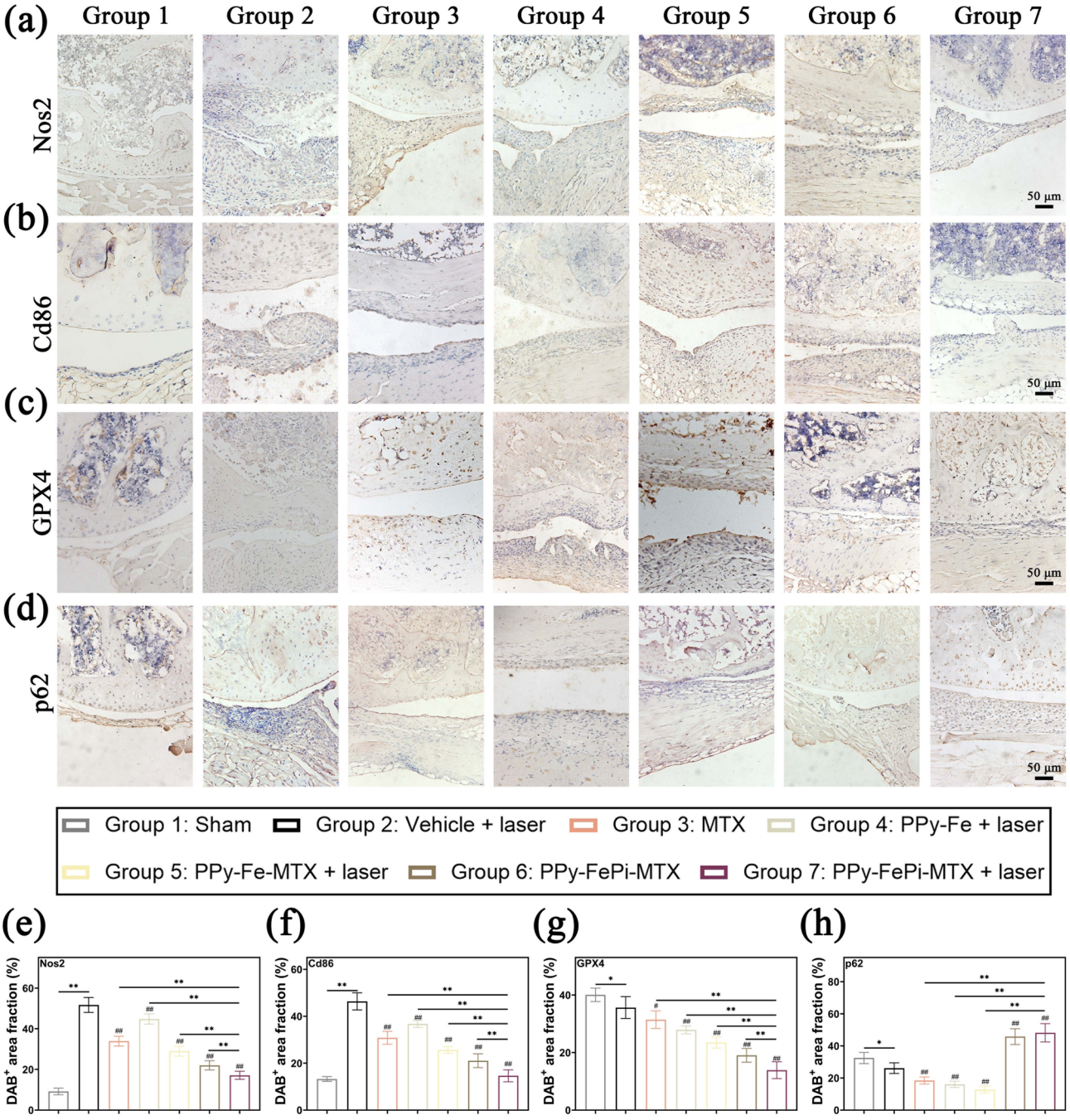

Fig. 9 Immunohistochemical staining for (**a**) Nos2, (**b**) Cd86, (**c**) GPX4, and (d) p62 in joint tissues from various groups. Scale bar: 50 μm. Statistical analysis of (**e**) Nos2 staining, (**f**) Cd86 staining, (**g**) GPX4 staining, and (**h**) p62 staining. # indicate significant differences in comparison to group 2. $^{\#,*}p < 0.05$, $^{\#\#,**}p < 0.01$

compared to other treatments (Fig. 8d and h). The data presented above indicated that PPy-FePi-MTX NPs had the potential to effectively reduce the development of RA by diminishing synovial inflammation, cartilage degradation, and bone erosion in CIA mice.

To evaluate biocompatibility, we assessed hepatotoxicity by measuring serum levels of the liver enzymes alanine transaminase (ALT) and aspartate aminotransferase (AST) post-treatment (Fig. S9a and S9b). Nephrotoxicity was evaluated by determining blood urea nitrogen (BUN) and creatinine (Cre) levels (Fig. S9c and S9d). The findings revealed no significant alterations in these parameters among groups 2, 3, 4, 5, 6, and 7, as compared to group 1, indicating minimal hepatic and renal toxicity.

Conclusions

In summary, a multifunctional PPy-FePi-MTX NP was prepared for effective RA treatment through an autophagy blockage-enhanced apoptosis/ferroptosis strategy. The payloads on PPy NPs were released under the stimulation of an inflammatory microenvironment. The released MTX, as well as the photothermal effect of PPy under NIR laser irradiation, directly induced M1 macrophage apoptosis. Fe^{3+} reacted with GSH to form Fe^{2+}, which converted H_2O_2 into cytotoxic ·OH. This redox process depleted glutathione, inactivated glutathione peroxidase 4, and caused lipid peroxidation accumulation, thereby resulting in ferroptosis of inflammatory M1 macrophages. Notably, PO_4^{3-} disrupted the normal function of lysosomes by pH disturbance, disabling the cytoprotective autophagy of M1 macrophages for augmented anti-RA efficacy. When injected intraarticularly into a mouse model of RA, these PPy-FePi-MTX NPs displayed significant anti-RA therapeutic effects. Therefore, the PPy-FePi-MTX NPs reported herein hold promising potential in the clinical management of RA.

Supplementary Information

The online version contains supplementary material available at https://doi.org/10.1186/s12951-025-03501-z.

Supplementary Material

Acknowledgements

ZAL acknowledges the support from the Chinese University of Hong Kong via the Vice-Chancellor Early Career Professorship Scheme.

Author contributions

Hui Liu: Writing-review & editing, Supervision, Conceptualization. Haoyu Wan: Writing-original draft & editing, Investigation, Data curation. Anbiao Zhang: Data curation, Investigation. Yi Ouyang: Writing-original draft, Investigation. Xinya Lu: Investigation. Mengyuan Wu: Investigation. Ning Hu: Funding acquisition. Jianying Pan: Writing-review & editing, Conceptualization, Data curation. Dong Guo: Writing-original draft & editing, Writing-review & editing, Data curation. Zhong Alan Li: Investigation, Data curation, Writing-review & editing. Denghui Xie: Writing-review & editing, Funding acquisition, Supervision, Conceptualization.

Funding

For this project was provided by the National Natural Science Foundation of China (No. 81974328, 82372358, 82072443, and 82372425), the Natural Science Foundation for Distinguished Young Scholars of Guangdong Province (2022B1515020044), the Natural Science Foundation of Guangdong Privince (2022A1515012562), and Guangdong Students' Platform for Innovation and Entrepreneurship Training Program (S202312121083). ZAL acknowledges the support from the Chinese University of Hong Kong via the Vice-Chancellor Early Career Professorship Scheme.

Data availability

No datasets were generated or analysed during the current study.

Declarations

Competing interests

The authors declare no competing interests.

Received: 29 December 2024 / Accepted: 27 May 2025

Published online: 07 June 2025

References

1. Scherer HU, Häupl T, Burmester GR. The etiology of rheumatoid arthritis. J Autoimmun. 2020;110:102400.
2. Alivernini S, Firestein GS, McInnes IB. The pathogenesis of rheumatoid arthritis. Immunity. 2022;55:2255–70.
3. Schett G, Gravallese E. Bone erosion in rheumatoid arthritis: mechanisms, diagnosis and treatment. Nat Rev Rheumatol. 2012;8:656–64.
4. Jang S, Kwon E-J, Lee JJ. Rheumatoid arthritis: pathogenic roles of diverse immune cells. Int J Mol Sci. 2022;23:905.
5. McInnes IB, Schett G. Cytokines in the pathogenesis of rheumatoid arthritis. Nat Rev Immunol. 2007;7:429–42.
6. Hazes JMW, Luime JJ. The epidemiology of early inflammatory arthritis. Nat Rev Rheumatol. 2011;7:381–90.
7. Gao W, Wang X, Zhou Y, Wang X, Yu Y. Autophagy, ferroptosis, pyroptosis, and necroptosis in tumor immunotherapy. Sig Transduct Target Ther. 2022;7:196.
8. Lei G, Zhuang L, Gan B. Targeting ferroptosis as a vulnerability in cancer. Nat Rev Cancer. 2022;22:381–96.
9. Yang J, Hu S, Bian Y, Yao J, Wang D, Liu X, Guo Z, Zhang S, Peng L. Targeting cell death: pyroptosis, ferroptosis, apoptosis and necroptosis in osteoarthritis, front. Cell Dev Biol. 2022;9:789948.
10. Chen H, Luo X, Huang Q, Liu Z, Lyu M, Chen D, Mo J, Zhu D. Platelet membrane fusion liposome loaded with type I AIE photosensitizer to induce chemoresistance cancer pyroptosis and Immunogenic cell death for enhancing cancer immunotherapy. Chem Eng J. 2023;476:146276.
11. Huang R, Zhang C, Bu Y, Li Z, Zheng X, Qiu S, Machuki JO, Zhang L, Yang Y, Guo K, Gao F. A multifunctional nano-therapeutic platform based on octahedral yolk-shell Au nr@cus: photothermal/photodynamic and targeted drug delivery tri-combined therapy for rheumatoid arthritis. Biomaterials. 2021;277:121088.
12. Wu X, Cao G, Chen H, Sheng W, Lv S, Li Z, Bai Z, Hua Z, Qiu Z, Chao M, Guo K, Zheng X, Gao F. Fenton/Fenton-like microreactor in inflammatory microenvironment: photothermal enhanced catalytic oxidation strategy for chemodynamic treatment of rheumatoid arthritis. Chem Eng J. 2023;474:145765.
13. Zheng X, Yang H, Zhang Z, Liang X, Liu Y, Wang C, Yang X, Tang J, Mao J, Nie Y, Zhou X, Li C. pH-responsive size-adjustable liposomes induce apoptosis of fibroblasts and macrophages for rheumatoid arthritis treatment. Acta Biomater. 2024;179:256–71.
14. Yang Y, Guo L, Wang Z, Liu P, Liu X, Ding J, Zhou W. Targeted silver nanoparticles for rheumatoid arthritis therapy via macrophage apoptosis and re-polarization. Biomaterials. 2021;264:120390.
15. Chen Z, Liu Z, Zhou Y, Rao K, Lin J, Zhu D, Ning S, Wang H. Bionic aggregation-induced emission photosensitizer for enhanced cancer immunotherapy. Mater Today Bio. 2024;28:101217.
16. Zhang N, Ping W, Xiang J, Chu S, Li D, Ning S, Zhu D, Zeng W, Xu Q. Biomimetic single-atom nanozyme for dual starvation-enhanced breast cancer immunotherapy. Adv Healthc Mater. 2024;14:2401362.
17. Scott J, Dixon KM, Lemberg MR, Lamprecht R, Skouta EM, Zaitsev CE, Gleason DN, Patel AJ, Bauer AM, Cantley WS, Yang B, Morrison BR, Stockwell. Ferroptosis: an iron-dependent form of nonapoptotic cell death. Cell. 2012;149:1060–72.
18. Jana D, Wang D, Bindra AK, Guo Y, Liu J, Zhao Y. Ultrasmall alloy nanozyme for ultrasound- and near-infrared light-promoted tumor ablation. ACS Nano. 2021;15:7774–82.
19. Long L, Guo H, Chen X, Liu Y, Wang R, Zheng X, Huang X, Zhou Q, Wang Y. Advancement in Understanding the role of ferroptosis in rheumatoid arthritis. Front Physiol. 2022;13:1036515.
20. Zhou Y, Fan S, Feng L, Huang X, Chen X. Manipulating intratumoral Fenton chemistry for enhanced chemodynamic and chemodynamic-synergized multimodal therapy. Adv Mater. 2021;33:2104223.
21. Yang Q, Zhang W, Lu S-Y, Cai X, Chen C, Zhang Q, Duan Y, Xie D, Zhang Q, Ran H, Liu H. Biodegradable doxorubicin-loaded ferric phosphate nanosheets for specific tumor elimination through autophagy inhibition-enhanced apoptosis/ferroptosis pathway. Chem Eng J. 2023;454:140455.
22. Meng X, Li D, Chen L, He H, Wang Q, Hong C, He J, Gao X, Yang Y, Jiang B, Nie G, Yan X, Gao L, Fan K. High-performance self-cascade pyrite nanozymes for apoptosis-ferroptosis synergistic tumor therapy. ACS Nano. 2021;15:5735–51.

23. Xi G, Hu X, Wu B, Jiang H, Young CYF, Pang Y, Yuan H. Autophagy Inhibition promotes paclitaxel-induced apoptosis in cancer cells. Cancer Lett. 2011;307:141–8.
24. Yang B, Ding L, Chen Y, Shi J. Augmenting tumor-starvation therapy by cancer cell autophagy Inhibition. Adv Sci. 2020;7:1902847.
25. Chen M, Yang D, Sun Y, Liu T, Wang W, Fu J, Wang Q, Bai X, Quan G, Pan X, Wu C. In situ self-assembly nanomicelle microneedles for enhanced photoimmunotherapy via autophagy regulation strategy. ACS Nano. 2021;15:3387–401.
26. Yang B, Ding L, Yao H, Chen Y, Shi J. A metal-organic framework (MOF) Fenton nanoagent-enabled nanocatalytic cancer therapy in synergy with autophagy Inhibition. Adv Mater. 2020;32:1907152.
27. Wan S-S, Zhang L, Zhang X-Z. An ATP-regulated ion transport nanosystem for homeostatic perturbation therapy and sensitizing photodynamic therapy by autophagy Inhibition of tumors. ACS Cent Sci. 2019;5:327–40.
28. Kato M, Ospelt C, Gay RE, Gay S, Klein K. Dual role of autophagy in stress-induced cell death in rheumatoid arthritis synovial fibroblasts. Arthritis Rheumatol. 2014;66:40–8.
29. Shin Y-J, Han S-H, Kim D-S, Lee G-H, Yoo W-H, Kang Y-M, Choi J-Y, Lee YC, Park SJ, Jeong S-K, Kim H-T, Chae S-W, Jeong H-J, Kim H-R, Chae H-J. Autophagy induction and CHOP under-expression promotes survival of fibroblasts from rheumatoid arthritis patients under Endoplasmic reticulum stress. Arthritis Res Ther. 2010;12:R19.
30. Li S, Chen JW, Xie X, Tian J, Deng C, Wang J, Gan HN, Li F. Autophagy inhibitor regulates apoptosis and proliferation of synovial fibroblasts through the Inhibition of PI3K/AKT pathway in collagen-induced arthritis rat model. Am J Transl Res. 2017;9:2065–76.
31. Xu L, Wang J, Wang J, Lu S-Y, Yang Q, Chen C, Yang H, Hong F, Wu C, Zhao Q, Cao Y, Liu H. Polypyrrole-iron phosphate-glucose oxidase-based nanocomposite with cascade catalytic capacity for tumor synergistic apoptosis-ferroptosis therapy. Chem Eng J. 2022;427:131671.
32. Geng H, Lupton EJ, Ma Y, Sun R, Grigsby CL, Brachi G, Li X, Zhou K, Stuckey DJ, Stevens MM. Hybrid polypyrrole and polydopamine nanosheets for precise raman/photoacoustic imaging and photothermal therapy. Adv Healthc Mater. 2023;12:2301148.
33. Gang F, Zhang Q, Jiang L, Xiao Y, Xu N, Wang Y, Xiao Y, Li A, Liu Z, Liu B, Wu Y, Su X, Perkins AG, Wu Q, Zhang J, Lin J, Sun X. Thermochemotherapy Meets tissue engineering for rheumatoid arthritis treatment. Adv Funct Mater. 2021;31:2104131.
34. Xiong H, Zhang H, Qin Y, Ye J, Zeng F, Xie P, Shi C, Luo C, Xu W, Yu C, Zhou Z, Chen X. Coassembly nanomedicine mediated by intermolecular interactions between methotrexate and baricitinib for improved rheumatoid arthritis treatment. ACS Nano. 2024;18:8337–49.
35. Ning S, Lyu M, Zhu D, Lam JW, Huang Q, Zhang T, Tang BZ. Type-I AIE photosensitizer loaded biomimetic system boosting Cuproptosis to inhibit breast cancer metastasis and Rechallenge. ACS Nano. 2023;17:10206–17.
36. Ning S, Zhang T, Lyu M, Lam JWY, Zhu D, Huang Q, Tang BZ. A type I AIE photosensitiser-loaded biomimetic nanosystem allowing precise depletion of cancer stem cells and prevention of cancer recurrence after radiotherapy. Biomaterials. 2023;295:122034.
37. Wang Z, Ren X, Li Y, Qiu L, Wang D, Liu A, Liang H, Li L, Yang B, Whittaker AK, Liu Z, Jin S, Lin Q, Wang T. Reactive oxygen species amplifier for apoptosis-ferroptosis mediated high-efficiency radiosensitization of tumors. ACS Nano. 2024;18:10288–301.
38. Liu Z, Liu S, Liu B, Bian Y, Yuan M, Yang C, Meng Q, Chen C, Ma Pa, Lin J. Fe(III)-naphthazarin metal–phenolic networks for glutathione-depleting enhanced ferroptosis–apoptosis combined cancer therapy. Small. 2023;19:2207825.
39. Ouyang Y, Li Y, Chen C, Zhao S, Wu M, Zhou B, Cao Y, Liu H. Copper phosphate-rotenone nanocomposites for tumor therapy through autophagy blockage-enhanced triphosadenine supply interruption and lipid peroxidation accumulation. Chem Eng J. 2024;495:153435.
40. Li W, Wang X, Wang J, Guo Y, Lu SY, Li CM, Kang Y, Wang ZG, Ran HT, Cao Y, Liu H. Enhanced photoacoustic and photothermal effect of functionalized polypyrrole nanoparticles for near-infrared theranostic treatment of tumor. Biomacromolecules. 2019;20:401–11.
41. Liu Y, Xu R, Gu H, Zhang E, Qu J, Cao W, Huang X, Yan H, He J, Cai Z. Metabolic reprogramming in macrophage responses. Biomark Res. 2021;9:1–17.
42. Cohn CA, Simon SR, Schoonen MAA. Comparison of fluorescence-based techniques for the quantification of particle-induced hydroxyl radicals, part. Fibre Toxicol. 2008;5:2.
43. Amaravadi RK, Kimmelman AC, Debnath J. Targeting autophagy in cancer: recent advances and future directions. Cancer Discov. 2019;9:1167–81.
44. Zhou W, Pan T, Cui H, Zhao Z, Chu PK, Yu XF. Black phosphorus: bioactive nanomaterials with inherent and selective chemotherapeutic effects. Angew Chem Int Ed. 2018;58:769–74.
45. Guan P, Meng Z, Liu X, Mu J, Gao Z, Yu X, Lian H. A biomimetic mineralization nanosystem based on glycolysis-oxidative stress-autophagy regulation for the suppression of malignant tumor and lung metastasis. Chem Eng J. 2023;468:143730.
46. Rius-Pérez S. p53 at the crossroad between mitochondrial reactive oxygen species and necroptosis. Free Radical Bio Med. 2023;207:183–93.
47. Li H, Wang P, Yu J, Zhang L. Cleaving Beclin 1 to suppress autophagy in chemotherapy-induced apoptosis. Autophagy. 2014;7:1239–41.
48. Komatsu M, Kageyama S, Ichimura Y. p62/SQSTM1/A170: physiology and pathology. Pharmacol Res. 2012;66:457–62.
49. Wang T, Zhang L, Hu J, Duan Y, Zhang M, Lin J, Man W, Pan X, Jiang Z, Zhang G, Gao B, Wang H, Sun D. Mst1 participates in the atherosclerosis progression through macrophage autophagy Inhibition and macrophage apoptosis enhancement. J Mol Cell Cardiol. 2016;98:108–16.
50. Wang Q, Zeng P, Liu Y, Wen G, Fu X, Sun X. Inhibition of autophagy ameliorates atherogenic inflammation by augmenting apigenin-induced macrophage apoptosis. Int Immunopharmacol. 2015;27:24–31.
51. Geng W, Zhao J, Tao B, Yang Y, Duan Q, Gao P, He T, Liu S, Feng Q, Zhao P, Cai K. Regulation of rheumatoid arthritis microenvironment via a self-healing injectable hydrogel for improved inflammation elimination and bone repair. Bioact Mater. 2024;36:287–300.
52. Brand DD, Latham KA, Rosloniec EF. Collagen-induced arthritis. Nat Protoc. 2007;2:1269–75.
53. Dai R, Zhao M, Zheng X, Li D, Kang W, Hao H, Chen X, Jin Y, Li J, Liu Q, Zheng Z, Zhang R. Homology-activated ultrasensitive nanomedicines for precise NIR-II FL/MRI imaging-guided knock-on dynamic therapy in rheumatoid arthritis. Adv Healthc Mater. 2024;13:2303892.
54. Qiu S, Wu X, Li Z, Xu X, Wang J, Du Y, Pan W, Huang R, Wu Y, Yang Z, Zhou Q, Zhou B, Gao X, Xu Y, Cui W, Gao F, Geng D. A smart nanoreactor based on an O_2-economized dual energy Inhibition strategy armed with dual multi-stimuli-responsive doorkeepers for enhanced CDT/PTT of rheumatoid arthritis. ACS Nano. 2022;16:17062–79.
55. Pandey PK, Maheshwari R, Raval N, Gondaliya P, Kalia K, Tekade RK. Nanogold-core multifunctional dendrimer for pulsatile chemo-, photothermal- and photodynamic- therapy of rheumatoid arthritis. J Colloid Interf Sci. 2019;544:61–77.
56. Guo D, Lin C, Lu Y, Guan H, Qi W, Zhang H, Shao Y, Zeng C, Zhang R, Zhang H, Bai X, Cai D. FABP4 secreted by M1-polarized macrophages promotes synovitis and angiogenesis to exacerbate rheumatoid arthritis. Bone Res. 2022;10:45.
57. Matsuzawa-Ishimoto Y, Hwang S, Cadwell K. Autophagy and inflammation. Annu Rev Immunol. 2018;36:73–101.
58. Guo D, Pan H, Lu X, Chen Z, Zhou L, Chen S, Huang J, Liang X, Xiao Z, Zeng H, Shao Y, Qi W, Xie D, Lin C. Rspo2 exacerbates rheumatoid arthritis by targeting aggressive phenotype of fibroblast-like synoviocytes and disrupting chondrocyte homeostasis via Wnt/β-catenin pathway. Arthritis Res Ther. 2023;25:217.
59. Li Y-N, Chen C-W, Trinh-Minh T, Zhu H, Matei A-E, Györfi A-H, Kuwert F, Hubel P, Ding X, Manh CT, Xu X, Liebel C, Fedorchenko V, Liang R, Huang K, Pfannstiel J, Huang M-C, Lin N-Y, Ramming A, Schett G, Distler JHW. Dynamic changes in O-GlcNAcylation regulate osteoclast differentiation and bone loss via nucleoporin 153. Bone Res. 2022;10:51.
60. Hascoët E, Blanchard F, Blin-Wakkach C, Guicheux J, Lesclous P, Cloitre A. New insights into inflammatory osteoclast precursors as therapeutic targets for rheumatoid arthritis and periodontitis. Bone Res. 2023;11:26.

Publisher's note